

arXiv:2601.11964v1 [physics.flu-dyn] 17 Jan 2026

Minimal seed in supersonic boundary layer at $M = 3$

Nobutaka Taniguchi and Aiko Yakeno

Institute of Fluid Science, Tohoku University

(Dated: January 21, 2026)

Abstract

This study investigates the minimal seed for laminar-to-turbulent transition in a supersonic boundary layer at $M = 3.0$ and $Re = 300$ using adjoint-based nonlinear non-modal analysis. While linear theory identifies oblique waves as the optimal disturbances for transient growth, we demonstrate that nonlinear effects fundamentally alter the optimal perturbation structure as the initial amplitude exceeds a critical threshold. Our analysis reveals that the nonlinear optimal perturbation exhibits a distinctive spatial distribution characterized by flattened structures in the outer layer and streamwise vortices near the wall, leading to a more rapid transition compared to the linear counterpart. A key finding is that this nonlinear amplification mechanism remains robust even under wall-cooled conditions ($T_w = 0.6T_{ad}$), where the disappearance of the generalized inflection point (GIP) suppresses linear instabilities of Mack's first mode. This rapid growth is driven by the nonlinear interaction between two-dimensional planar waves near the wall and staggered vortex patterns in the outer layer, facilitating streak formation through vortex self-induction. Although the late-stage evolution eventually converges to the classical oblique breakdown scenario as characterized by the formation of Λ -vortices, the identified nonlinear path significantly reduces the disturbance energy required for transition.

I. INTRODUCTION

The existence of inviscid instability is a key characteristic of the transition process in compressible boundary layers. The mathematical basis for compressible instabilities was established by Lees & Lin [1] and Lees & Reshotko [2]. In their pioneering studies, inviscid instabilities were classified into subsonic, sonic, and supersonic modes depending on the phase speed relative to the local speed of sound, which leads to essential differences in the treatment of boundary-value problems. Lees & Lin [1] showed that the necessary condition for a neutral subsonic mode in compressible flow is the existence of a Generalized Inflection Point (GIP) inside the boundary layer, while the condition for supersonic instability remained unestablished at that time. The characteristics of the supersonic instabilities of the compressible boundary layer have been extensively investigated via numerical calculations [3, 4] and later in experiments [5]. It is widely accepted that the compressible boundary layer at moderate Mach number (up to Mach number $M \approx 4.5$ at an adiabatic wall

temperature in [3]) exhibits subsonic instability associated with Mack's first mode, which becomes most unstable at an oblique wave angle. For higher Mach number, two-dimensional instability of Mack's second mode becomes the most unstable mode among the multimodal solutions of neutral supersonic modes.

These compressible linear instabilities lead to several transition scenarios depending on the Mach number. At low Mach numbers, transition paths originating from oblique waves have been identified. Oblique breakdown [6–9] is a unique transition scenario which is initiated by a pair of oblique waves with equal and opposite angles without undergoing the evolution of secondary instability, which is also reported in incompressible transition [10]. On the other hand, the transition path via secondary instability of the primary mode, including subharmonic resonance [11] and asymmetric subharmonic [12, 13] resonance have been identified in supersonic boundary layer. At higher Mach number, the subharmonic resonance of Mack's second mode was confirmed ([14]). More recently, Zhu et al. [15] experimentally investigated the laminar-turbulence transition which was initiated from the excitation of Mack's second mode, amplified by promoting low-frequency modes.

From the perspective of stability analysis, these transition scenarios are characterized by the linear amplification of disturbances and their subsequent nonlinear breakdown. It is well-established that the pseudospectra of the linear stability operator play a crucial role to analyze the transition process, as the non-normality of the operator induces transient amplification of the disturbance field [16, 17]. Hanifi et al. [18] applied linear non-modal analysis to the compressible boundary layer, assuming a locally parallel base flow. They demonstrated that the maximum amplification of disturbances is achieved via the lift-up effect originating from streamwise vortices, and that an increase of Mach number modifies the potential amplification. The spatial theory of optimal disturbances was conducted by Tumin and Reshotko [19], further supporting the finding that streamwise vortices cause significant disturbance growth. More recently, Bugeat et al. [20] applied global spatial analysis to the compressible boundary layer to construct an amplification map in the (ω, β) plane, where ω, β are the temporal frequency and spanwise wavenumber, where the growth rate of streaks and Mack's first and second modes were identified as local maxima.

As indicated by the existence of several transition scenarios, nonlinear interactions between linear instabilities and amplification mechanisms form the basis for understanding laminar-to-turbulent transition. From the perspective of flow control, variations in distur-

bance growth in the presence of steady streaks and blowing/suction have been investigated by Paredes et al. [21] and Poulain et al. [22]. Within the general framework of finite-amplitude disturbances, nonlinear non-modal analysis provides crucial clues regarding nonlinear amplification [23, 24]. The fundamental idea of this analysis, the concept of "minimal seed" [24, 25] (i.e. the least-energy solution that triggers transition), is widely accepted, particularly for incompressible flows. For incompressible boundary layers, Cherubini et al. [25] found that a self-sustaining process (SSP) involving a disturbance-regeneration cycle persists across multiple scales during transition. However, studies addressing finite-amplitude disturbances in compressible flows remain insufficiently examined. Huang and Hack [26] applied nonlinear non-modal analysis to subsonic pipe flow to investigate Mach number effects on optimal perturbations, though its relationship with inviscid instability was not discussed. Jahanbakhshi and Zaki [27] conducted an ensemble-variational approach of nonlinear non-modal analysis of a supersonic boundary layer at $M = 4.5$. They reported that the least-energy transition path is attributed to the coupling of acoustic modes (Mack's second mode) and oblique mode. At the same Mach number but a slightly higher Reynolds number, Zhou et al. [28] performed nonlinear parabolized stability equations (NPSE) analysis, revealing the nonlinear interactions between oblique first and second modes induce significant disturbance amplification. More recently, a nonlinear resolvent analysis framework was proposed by Rigas et al. [29], revealing critical nonlinear resonances in compressible boundary layers [22, 29]. Nevertheless, existing studies primarily focus on high Reynolds numbers where multiple transition processes coexist, leaving the nonlinear disturbance amplification mechanisms in the subcritical regime of compressible boundary layers insufficiently explored.

The purpose of this study is to obtain the minimal seed of supersonic boundary layer at $M = 3.0$ for subcritical Reynolds number and to investigate its mechanism to trigger the laminar-to-turbulence transition. In particular, we investigate how the change of self-sustaining process (SSP) structure identified by Cherubini et al. [25] for incompressible boundary layer is modified in a presence of compressibility and Mack's modes in supersonic boundary layer.

II. METHODOLOGY

A. Governing equation

The governing equations are the non-dimensionalized compressible Navier–Stokes (N–S) equations, expressed as follows:

$$\partial_t \rho + u_j \partial_j \rho = -\rho \partial_j u_j, \quad (1)$$

$$\partial_t m_i + \partial_j (u_j m_i) = -\partial_i p + \partial_j \tau_{ij}, \quad (2)$$

$$\partial_t p + \partial_j (p u_j) = -\tilde{\gamma} (p \partial_j u_j - \tau_{ij} \partial_j u_i + \partial_j \Theta_j), \quad (3)$$

where $\rho, m_x, m_y, m_z, p, T$ represent the density, momentum components in the x, y, z directions, pressure, and temperature. For non-dimensionalization, we adopt the Blasius length scale l at a reference location and the freestream density ρ_e , velocity U_e , temperature T_e , and the coefficient of viscosity μ_e as reference quantities. We set the reference location from the leading edge, x_0 , and the Blasius length and Reynolds number is defined as

$$l = \sqrt{\frac{\mu_e x_0}{U_e}}, \quad Re = \frac{\rho_e U_e l}{\mu_e}. \quad (4)$$

The viscous stress tensor is defined as

$$\tau_{ij} = \frac{\mu}{Re} \left(\partial_j u_i + \partial_i u_j - \frac{2}{3} \delta_{ij} \partial_k u_k \right), \quad (5)$$

under Stokes' hypothesis. The heat flux vector is given by

$$\Theta_i = -\frac{\kappa}{\tilde{\gamma} M^2 Re Pr} \partial_i T, \quad (6)$$

where Re is the Reynolds number, M is the Mach number, Pr is the Prandtl number, γ is the specific heat ratio, and $\tilde{\gamma} = \gamma - 1$. To close the system of equations, the state equation is given in non-dimensional form as

$$p = \frac{\rho T}{\gamma M^2}. \quad (7)$$

In the above equations, μ, κ denote the coefficient of viscosity and thermal conductivity, respectively. Specifically, we set $Pr = 0.7$ and $\gamma = 1.4$ by assuming a standard atmosphere composition. The coefficient of viscosity is modeled using Sutherland's law. The reference temperature for the model equations is set to the freestream temperature, corresponding to a stagnation temperature of $600^{\circ}R$ (333 [K]) following the recommendation of Malik et al. (1990) [30]. Specific physical parameters, including the reference length x_0 and reference temperature T_e , are described in detail in the subsequent section on flow conditions.

B. Nonlinear non-modal analysis

The methodology of nonlinear non-modal analysis has been well established in the studies by Cherubini et al. [23] and Pringle and Kerswell [24]. Our implementation is based on our previous study [31], with slight modifications in the selection of evaluation function and the update procedure for the spatial distribution of the initial disturbance. In this analysis, the total flow field $\mathbf{q} = \mathbf{q}(t, \mathbf{x})$ is decomposed into a steady base flow $\mathbf{Q} = \mathbf{Q}(\mathbf{x})$ and a disturbance flow field $\mathbf{q}' = \mathbf{q}'(t, \mathbf{x})$ as

$$\mathbf{q}(t, \mathbf{x}) = \mathbf{Q}(\mathbf{x}) + \mathbf{q}'(t, \mathbf{x}). \quad (8)$$

The base flow \mathbf{Q} is assumed to be a steady solution to the compressible Navier–Stokes (N–S) equations. The evolution of the perturbed flow is treated as an initial value problem, where the initial state is given by

$$\mathbf{q}(0, \mathbf{x}) = \mathbf{Q}(\mathbf{x}) + \hat{\mathbf{q}}_0. \quad (9)$$

Here, $\hat{\mathbf{q}}_0 = \mathbf{q}'(0, \mathbf{x})$ denotes the initial disturbance, which is the subject of optimization in the nonlinear non-modal analysis. The state vector is defined as $\mathbf{q} = (\rho, m_x, m_y, m_z, p)^{\text{tr}}$. To distinguish these components, the base flow and disturbance fields are denoted as $\mathbf{Q} = (\bar{\rho}, \bar{m}_x, \bar{m}_y, \bar{m}_z, \bar{p})^{\text{tr}}$ and $\mathbf{q}' = (p', m'_x, m'_y, m'_z, p')^{\text{tr}}$.

The Cartesian coordinate system is defined such that x , y , and z correspond to the streamwise, wall-normal, and spanwise directions, respectively. The origin in the xy -plane is located at the leading edge of the wall, while the origin of the z -coordinate is set arbitrarily.

Under this configuration, the objective of the nonlinear non-modal analysis is to optimize the initial disturbance field $\hat{\mathbf{q}}_0$ field to achieve maximum amplification at the evaluation time $t = t_f$. To quantify the disturbance magnitude, we introduce an evaluation function representing the disturbance energy for the compressible flow field as

$$E(t) := \frac{1}{2} \int_{\Omega} \frac{\bar{p}}{\bar{\rho}^2} \rho'^2 + \frac{1}{\bar{\rho}} m'_i m'_i + \frac{\bar{\rho}}{\gamma \tilde{\gamma} \bar{T} M^2} T'^2 dV \quad (10)$$

where Ω denotes the calculation domain. The definition in (10) is a modification of the norm by Hanifi et al. [18], adapted for our selection of fundamental variables (i.e. momentum density instead of velocity). The optimization maximizes the disturbance amplitude at $t = t_f$ under the constraint of a constant initial disturbance magnitude, $E(0) = \delta^2$, and the condition that the perturbed flow field satisfies the compressible N–S equations as

$$\partial_t \mathbf{q} = \mathcal{F}[\mathbf{q}] \quad (11)$$

where \mathcal{F} symbolically represents the right-hand-side of the governing equations.

Based on these conditions, the Lagrange multiplier method is applied to optimize disturbance amplification under the prescribed constraints. The resulting Lagrangian functional is defined as

$$\mathcal{L} = E(t_f) - \nu(E(0) - \delta^2) - \int_0^{t_f} \langle \boldsymbol{\lambda}, \partial_t \mathbf{q} - \mathcal{F}[\mathbf{q}] \rangle dt \quad (12)$$

where $\nu, \boldsymbol{\lambda}$ are the Lagrange multipliers, and the brackets \langle, \rangle denote the standard L_2 inner product.

The spatial distribution of the optimal perturbation is updated using the steep-ascent method. By taking the first variation of \mathcal{L} with respect to the state vector \mathbf{q} and the multipliers, we obtain the Euler–Lagrangian equations, which comprise the compressible N–S equations and their corresponding adjoint equations [32]. The terminal condition for the adjoint vector at $t = t_f$ is given by

$$\boldsymbol{\lambda}(t_f) = \left(\frac{\partial E(t_f)}{\partial \mathbf{q}(t_f)} \right)^{\text{tr}}, \quad (13)$$

where the gradient of the energy functional $\partial E / \partial \mathbf{q}$ is derived as

$$\frac{\partial E}{\partial \mathbf{q}} = \left(C_p \frac{\bar{T}}{\bar{\rho}} \rho' - \frac{p'}{\tilde{\gamma} \bar{\rho}}, \frac{m'_x}{\bar{\rho}}, \frac{m'_y}{\bar{\rho}}, \frac{m'_z}{\bar{\rho}}, C_v \frac{\bar{\rho}}{\bar{p}} T' \right)^{\text{tr}}. \quad (14)$$

where $C_v = 1/(\tilde{\gamma} \gamma M^2)$ and $C_p = \gamma C_v$.

The variation of the Lagrangian with respect to the initial disturbance field requires careful treatment in compressible case. The variation with respect to $\mathbf{q}(0)$ yields

$$\left\langle -\boldsymbol{\lambda}(0) + \mu \frac{\partial E(0)}{\partial \mathbf{q}(0)}, \delta \mathbf{q}(0) \right\rangle = 0, \quad (15)$$

and the variation with respect to ν recovers the initial energy constraint. Since the disturbance energy is a quadratic form, we can introduce a weight matrix $A = A(\mathbf{Q})$ such that $\partial E(0) / \partial (\hat{\mathbf{q}}_0) = A(\mathbf{Q}) \hat{\mathbf{q}}_0$. Consequently, the initial disturbance satisfying (15) is obtained as

$$\hat{\mathbf{q}}_0 = \mu^{-1} A^{-1} \boldsymbol{\lambda}(0) \quad (16)$$

where the invertibility of A is guaranteed by the positive-definiteness of the energy norm defined in (10). From $E(0) = \delta^2$ and (16), the multiplier ν can be uniquely determined. This approach differs significantly from the incompressible case, where A simplifies to an identity matrix. While various treatments of ν are common in incompressible optimization

[33, 34], compressible flow necessitates this rigorous treatment of A to ensure consistency. Finally, the initial disturbance field is updated as

$$\hat{\mathbf{q}}_0^{(n+1)} = \hat{\mathbf{q}}_0^{(n)} - \epsilon^{(n)} \left(-\boldsymbol{\lambda}^{(n)}(0) + \nu^{(n)} \left(\frac{\partial E(0)}{\partial \mathbf{q}(0)} \right)^{(n)} \right), \quad (17)$$

where n denotes the optimization process number. Here, ϵ is the step width which is empirically determined following the strategies of Pringle and Kerswell [33].

C. Flow configurations

For the problem setup, we consider a laminar supersonic boundary layer at $M = 3.0$. The inflow boundary of the computational domain is set at $x = 0$, while the leading edge of the flat plate is located at $x = -300$. The characteristic length for the non-dimensionalization is taken as $x_0 = 300$ between these points. The wall-normal profile at this location is obtained via a precursor calculation. The computational domain for the nonlinear non-modal analysis was defined as $[x, y, z] \in [0, 450] \times [0, 100] \times [-25, 25]$. The spanwise extent is chosen to accommodate two periods of the most amplified mode reported by Hanifi et al. (1996) [18]. To obtain an inflow condition at $x = 0$, several numerical techniques are employed to mitigate the influence of weak shock waves originating from the leading-edge region. In the precursor calculation, shock wave reflections at the far-field boundary are suppressed using the localized artificial diffusivity (LAD) method by Kawai and Lele (2008) [35] and a sponge layer [36] applied for $20 \leq y$. Notably, neither LAD method nor sponge layers are applied for the nonlinear non-modal analysis and the time-evolution of perturbed flow to preserve the accuracy of the results. For the subsequent analysis of the perturbed flow field, the domain is extended in the streamwise direction to $x \in [0, 900]$ to track the complete nonlinear process of laminar-to-turbulent transition.

Regarding the wall boundary conditions, an isothermal condition is applied. The wall temperature T_w is set to either $T_w = T_{ad}$ or $0.6T_{ad}$, where T_{ad} denotes the adiabatic wall temperature obtained from the self-similarity solution of the boundary layer equations. A far-field boundary condition is imposed at the top boundary ($y = 100$), while an outflow boundary condition is applied at $x = 450$ for the optimization process and at $x = 900$ for the transition tracking. Periodic boundary conditions are imposed in the spanwise direction at $z = \pm 25$.

D. Numerical discretization methods

Spatial derivatives are evaluated using a sixth-order compact finite difference scheme [37]. To suppress numerical instabilities of aliasing arising from poorly resolved high-frequency modes, a tenth-order compact filtering method [38] ($\alpha_f = 0.45$ for the intensity of filtering) is applied. Time integration is performed using a third-order Total Variation Diminishing (TVD) Runge–Kutta scheme [39].

The computational domain for the nonlinear non-modal analysis is discretized with a grid of $512 \times 256 \times 128$ points in the streamwise (x), wall-normal (y), and spanwise (z) directions, respectively. Uniform grid spacing is employed in the streamwise and spanwise directions, with $\Delta x = 0.879$ and $\Delta z = 0.391$. In the wall-normal direction, the grid is clustered near the wall surface; the minimum spacing is $\Delta y_{\min} = 0.0648$, which corresponds to approximately 1.2% of the displacement thickness δ^* under adiabatic wall conditions. This spatial resolution is verified to be sufficient for resolving the characteristic wavelengths of Mack’s first and second modes, as well as the resulting nonlinear interactions.

E. Numerical validation

To validate the current numerical framework, the nonlinear optimal perturbations are computed in the incompressible limit and compared against the results of Cherubini et al. (2011) [25] (hereafter referred as CPRB). To match the problem setup in the literature, the computational domain is set to $[0, 200] \times [0, 20] \times [0, 10.5]$, normalized by the boundary-layer thickness δ at the corresponding Mach number. The calculation domain is discretized using a grid of $768 \times 128 \times 64$ points, which is approximately the same resolution with CPRB.

The flow parameter is selected $Re_\delta = 300$ based on the boundary layer thickness at $M = 0.4$. Note that CPRB defines the disturbance energy as the L^2 norm of velocity magnitude (without the $1/2$ factor commonly used in kinetic energy definitions). Therefore, our energy definition in (10) is multiplied by a factor of 2 to ensure a consistent comparison. The initial disturbance magnitude is set to $\delta = 0.1$, following the parameter in CPRB. Figure 1 shows the comparison results and it shows a good agreement particularly for the short evaluation time $t_f = 25$. In contrast, for the long evaluation time $t_f = 100$, the current result underestimates the growth rate of the disturbance field by 29% compared to the value

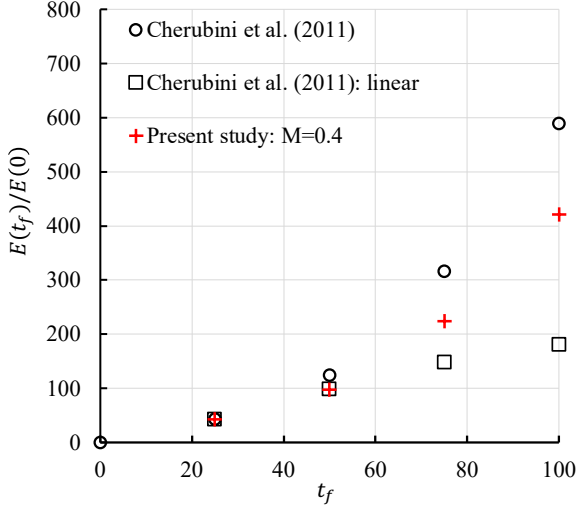


FIG. 1: Comparison of growth rate of nonlinear non-modal analysis at incompressible limit ($M = 0.4$) with the literature values.

reported by CPRB. This deviation is likely attributable to the inherent compressibility at $M = 0.4$. As discussed by Chang and Malik [6], compressibility tends to suppress the growth rate of disturbances compared to the purely incompressible limit. Despite these differences, the present numerical framework successfully captures the structural characteristics of the nonlinear optimal perturbation.

III. BASE FLOW

The base flow is obtained by solving the steady two-dimensional compressible N–S equations under the aforementioned flow conditions. Figure 2 compares the wall-normal profiles of velocity and temperature at the inflow boundary with the self-similar solution. The self-similarity solution is derived from the compressible boundary layer equations using the Illingworth transformation, following the methodology in White [40]. This solution was validated by comparing the displacement thickness with the result of Malik [30].

The figure demonstrates excellent agreement between the computed base flow and the self-similar solution. Outside the boundary layer, slight deviations from the uniform flow are observed, which are attributed to weak shock waves originating from the leading edge; these effects could not be entirely eliminated even with the sponge layer. However, since these deviations are located sufficiently far from the wall, their influence on the optimal per-

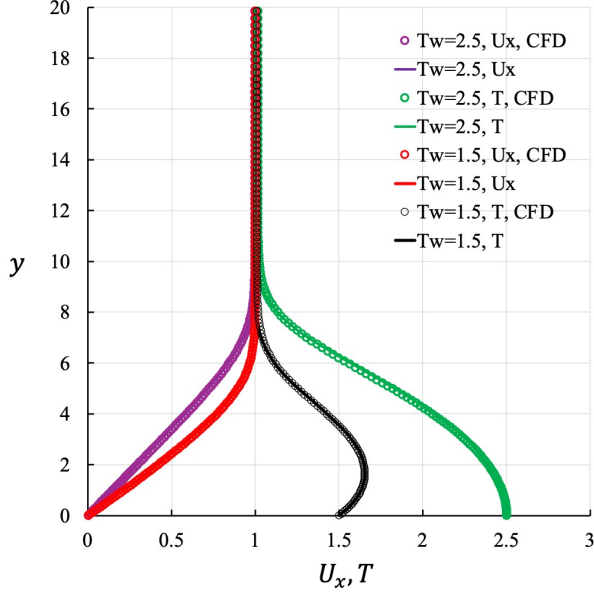


FIG. 2: Comparison of wall-normal profiles at the inflow boundary for $T_w = T_{ad}, 0.6T_{ad}$: numerical calculation (open circles) versus self-similar solution (lines).

turbation is negligible. Therefore, the base flow used in this analysis accurately reproduces the properties of a compressible boundary layer.

Wall cooling reduces the temperature within the boundary layer, shifting the location of the maximum temperature further from the wall. This temperature reduction decreases the local viscosity via Sutherland's law, resulting in a thinner boundary layer. Consequently, the displacement thickness decreases by 32.2%, from 5.40 at $T_w = T_{ad}$ to 3.66 at $T_w = 0.6T_{ad}$. This modification of the base flow is expected to significantly alter the linear stability characteristics, particularly by eliminating the GIP.

IV. NUMERICAL RESULTS

A. Optimization properties

First, we investigate the convergence properties of the optimization process. Figure 3 illustrates a typical optimization history in the present study. Here, the residuals are normalized by the volume of computational domain and the magnitude of the initial disturbance field. During the optimization, the residual of the steep-ascent method exhibits significant oscillations, which results from the adaptive adjustment of the step width designed to accel-

erate convergence. Indeed, these numerical oscillations in the residual can be suppressed by omitting the step-width acceleration strategy proposed by Pringle and Kerswell [33]. However, such a modification would require a significantly larger number of iterations to reach the maximum value.

As shown in the figure, the residual in the optimization process correlates with the update magnitude of the evaluation function. We consider the optimization to be converged when the residual falls below 5×10^{-6} and the changes in disturbance growth is less than 0.01, which corresponds to approximately 0.001% changes of the evaluation functions. This threshold is deemed sufficient, as no significant changes in the spatial structure of the optimal perturbation were observed beyond this point.

B. Characteristics of optimal perturbations

The amplification of the disturbance growth is presented in Table I, where the gain is defined as

$$G(t_f, \delta) = \frac{E(t_f; \delta)}{E(0; \delta)}. \quad (18)$$

For simplicity, t_f is omitted from the notation when the evaluation time is clear from the context. Table I summarizes the obtained growth rates at the specific evaluation times. It is observed that the growth rate increases substantially with the magnitude of the initial

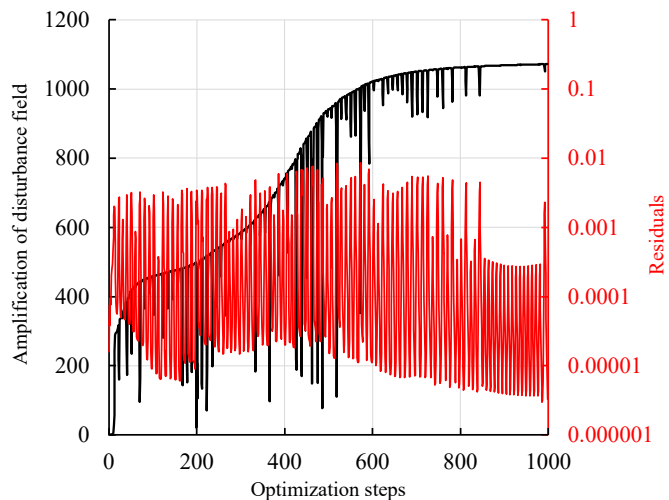


FIG. 3: Convergence of optimization process in the nonlinear non-modal analysis at $\delta = 1.0, t_f = 150, T_w = 0.6T_{ad}$.

TABLE I: Disturbance growth at the evaluation time and the spatial wavenumber for the linear optimal disturbance $\delta = 10^{-3}$.

t_f	T_w	$\delta = 1.0$	$\delta = 10^{-3}$			
		$G \times 10$	$G \times 10$	k_x	k_z	ψ
50	T_{ad}	270	310	0.439	0.00531	0.69°
100	T_{ad}	610	540	0.26	0.235	42.1°
150	T_{ad}	1380	800	0.154	0.253	58.7°
150	$0.6T_{ad}$	1070	510	0.124	0.247	63.3°

disturbance field δ . The condition $\delta = 10^{-3}$ is selected to represent the linear regime, where the disturbance intensity at $t = t_f$ remains sufficiently small to neglect nonlinear interaction effects. For the case of $t_f = 150$ and $T_w = T_{ad}$, linear amplification is still observed even at $\delta = 0.1$, yielding a growth rate of $G = 810$. As the initial amplitude increases, the growth rate is further enhanced by nonlinear effects, particularly for longer evaluation times.

The dominant wavenumbers in x, z directions were calculated from the linear optimal perturbation by assuming a normal mode distribution as $\hat{\mathbf{q}}_0(\mathbf{x}) = \tilde{\mathbf{q}}_0(y) \exp\{i(k_x x + k_z z)\}$. Based on this assumption, the effective wavenumbers are defined as

$$k_{x[z]}^2 = \frac{||\partial_{x[z]}\hat{\mathbf{q}}_0(\mathbf{x})||_2^2}{||\hat{\mathbf{q}}_0(\mathbf{x})||_2^2}. \quad (19)$$

The applicability of above equations can be justified by the fact that the perturbations are sufficiently narrow-banded in wavenumber space, as we will discuss in subsequent sections. The wave angle $\psi = \tan^{-1}(k_z/k_x)$, as presented in Table I. For a short evaluation time ($t_f = 50$), the optimal perturbation exhibits strong two-dimensionality with the streamwise wavenumber consistent with Mack's first mode. As t_f increases, k_x decreases, and the optimal perturbation characterizes oblique waves with $\psi = 58.7^\circ$ at $t_f = 150$, which is comparable to the unstable angle of 65° in linear stability theory (LST) [3]. However, for longer evaluation times, the growth rate and wavenumbers of the optimal perturbation, at least within the linear range, are expected to change further. Although Hanifi et al. [18] demonstrated that the global maximum amplification occurs for streamwise vortices ($k_x = 0$) when t_f is unconstrained, the present study specifically aims to elucidate the initial stage of nonlinear interactions leading to laminar-to-turbulent transition via oblique waves. There-

TABLE II: Disturbance growth at the evaluation time of the optimal perturbations with a different initial disturbance magnitude at $t_f = 150$.

δ	10^{-3}	0.1	0.25	0.4	0.5	0.75	1.0
G	800	810	840	1310	1370	1370	1380

fore, the selection of $t_f = 150$ is physically appropriate for capturing the targeted transition mechanism.

We also investigated the effect of cooled boundary on the amplification of the disturbance field especially at the case of $t_f = 150$. The amplification of disturbance growth was 510 at $\delta = 10^{-3}$ and 1070 at $\delta = 1.0$, representing a significant suppression of growth compared to the adiabatic wall temperature condition in Table I. This trend is consistent with expectations, as the disappearance of the GIP due to wall cooling suppresses the subsonic inviscid instability [3]. According to Table I, the amplification ratio was decreased by 36.3% in linear case and 22.5% in nonlinear case from $T_w = T_{ad}$ to $T_w = 0.6T_{ad}$. This ratio change suggests that while the linear growth is strongly mitigated by cooling, the nonlinear amplification mechanism remains robust and is not as significantly suppressed.

Table II summarizes the influence of the initial disturbance magnitude δ on the amplification of the optimal perturbation field. It is observed that the amplification increases monotonically from the linear limit (10^{-3}) for $\delta < 0.4$. In contrast, for $\delta \geq 0.4$, the amplification exhibits a discrete jump to $G = 13.7 \times 10^2$ and maintains this order of magnitude until numerical divergence occurs at $\delta = 2.0$. This step-like change in amplification differs significantly from the behavior for incompressible shear flow where continuous change in growth rate was observed by [41] (see Fig. 3 therein). This discrepancy suggests the existence of multiple transient paths from laminar to turbulent states, which causes the emergences of multiple optimal perturbations as δ increases, as discussed by Kerswell [42]. This sensitivity to the initial amplitude implies that a specific nonlinear mechanism becomes dominant once a critical threshold is exceeded, effectively skipping the preliminary nonlinear interactions characteristic of the low-amplitude regime ($\delta < 0.4$).

C. Spatial distribution of optimal perturbations

In this section, we investigate the spatial distribution characteristics of the optimal perturbations. As reported in previous nonlinear optimal perturbation analyses for both incompressible and compressible shear flows [25, 26], considering finite-amplitude effects leads to localization in the streamwise direction and modulation of the streamwise and spanwise wavelengths. Indeed, based on a local energy density criterion based on (10), the nonlinear optimal perturbation at $\delta = 1.0$ and $t_f = 150$ (defined as the region where intensity exceeds 2% of the maximum) is localized within $x \in [40, 150]$. In contrast, the linear optimal perturbation at $\delta = 10^{-3}, t_f = 150$ is distributed over a much wider range, $x \in [0, 320]$, under the same criterion. This locally concentrated structure was observed for large initial disturbance magnitude case to maintain the nonlinear structures of the optimal perturbation by increasing the local energy density. To further characterize these distributions, we extracted one-dimensional wall-normal profiles by averaging the disturbance fields in both the spanwise and streamwise directions. The streamwise averaging was performed over the specific intervals $[60, 80]$, $[80, 100]$, $[100, 120]$ and $[120, 140]$. The width of these windows was determined based on the streamwise wavelength of the linear optimal perturbation, as presented in Table I.

Figure 4 displays the extracted wall-normal distribution of the optimal perturbation field. In this figure, the velocity components are normalized by the initial disturbance amplitude. For the linear case ($\delta = 0.001$), the streamwise velocity component (u_x) becomes dominant and it concentrated in the intermediate region between the GIP ($(\rho U')' = 0$) and the location of maximum shear. This wall-normal profile remains invariant along the streamwise direction, with only negligible variations arising from the slight mismatch between the averaging interval and the primary wavelength. Since the present analysis focuses on a relatively short spatial range where the parallel flow approximation is applicable ($300 \leq Re \leq 474$), the resulting disturbance amplification is comparable to that predicted by the local theory of linear optimal perturbation. As the initial disturbance magnitude (δ) increases, however, the peak location and the mode shape of the streamwise velocity profile undergo subtle modification that varies depending on the averaging.

The concentration of the disturbance near the GIP suggests that this instability is related to the subsonic inviscid instability of the compressible boundary layer, consistent with clas-

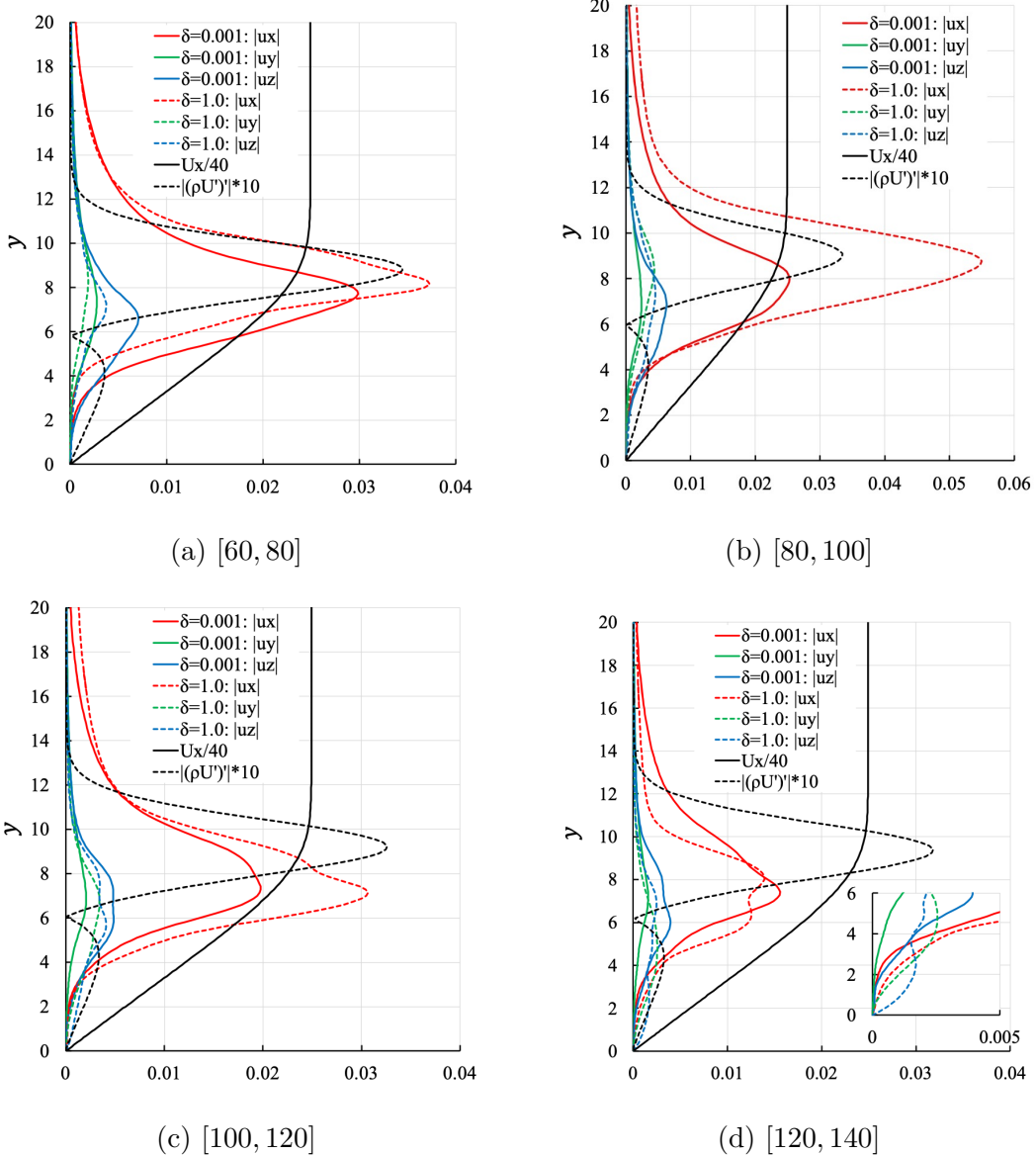


FIG. 4: Wall-normal distribution of optimal perturbation at $\delta = 0.001$ and $\delta = 1.0$ at $t_f = 150$ averaged spanwise and stream direction, where the streamwise average range is presented in each sub-caption of figures. Base flow statistics are presented in the black curves in the same manner in each figures with an appropriate scales for visualization.

sical theory [1]. Indeed, the wall-normal distribution in the linear case shows a high degree of similarity to the oblique wave distributions reported by Bugeat et al. (2019) [20] (see Fig. 11 therein) and Dwivedi et al. (2020) [43]. This similarity further supports the conclusion that dominant optimal growth mechanism is associated with the inviscid instability of Mack's first mode.

In contrast, nonlinear optimal perturbation ($\delta = 1.0$) exhibits a significant dependence on the streamwise direction and develops a complex three-dimensional structure. For $x \in [60, 80]$, the streamwise velocity u_x is concentrated near the location of maximum shear and its wall-normal distribution is shifted further away from the wall compared to the linear case. Moreover, because the nonlinear optimal perturbation is more spatially localized, its local intensity is significantly higher than that of the linear perturbation field (Fig. 4 (b)). Further downstream ($x \in [120, 140]$), the peak intensity at the location of maximum shear decreases, and the wall-normal distribution shifts toward the wall. Near the wall ($y \leq 4$), the wall-normal velocity u_y and spanwise velocity u_z shows a clear increase compared to the linear case, characterizing the formation of streamwise vortices, as discussed in the following subsection. This near-wall distribution of the optimal perturbation is critical, as it possesses high intensity relative to the base flow field.

Next, we investigate the spatial distribution of the optimal perturbations. Figure 5 displays the iso-contours of Q-criterion for the different initial disturbance magnitudes. For the linear case ($\delta = 10^{-3}$), the spatial distribution shows a high degree of similarity to those reported by Bugeat et al. [20] and Rigas et al. [29] (for the incompressible case), where the present analysis successfully reproduces the characteristics of the oblique forcing mode that triggers oblique breakdown. As the initial magnitude (δ) increases, the optimal perturbation initially exhibits a locally concentrated streamwise distribution, while its wall-normal characteristics, including a wave angle $\psi = 55^\circ$, are largely retained. Regarding the transition scenario, Rigas et al. [29] predicted that the resolvent forcing pattern extracts subharmonic breakdown in incompressible flows. The optimal perturbations before the step-like changes in Table II ($\delta < 0.5$) correspond to the secondary nonlinear effect of primary linear disturbance amplification.

With a further increase in the initial disturbance amplitude, the nonlinear optimal perturbation develops distinct features: flattened structures in the upper boundary layer and streamwise vortices in the lower boundary layer. This vorticity distribution exhibits a more complex three-dimensional arrangement in the wall-normal direction, as shown in Fig. 5 (c), whereas the linear optimal perturbation is distributed rather uniformly throughout the boundary layer. For larger initial disturbance magnitude, Cherubini et al. [25] noted that incompressible nonlinear optimal perturbations follow the oblique transition scenario, where nonlinear effects lead to a rapid amplification of the disturbance field. Compared to the in-

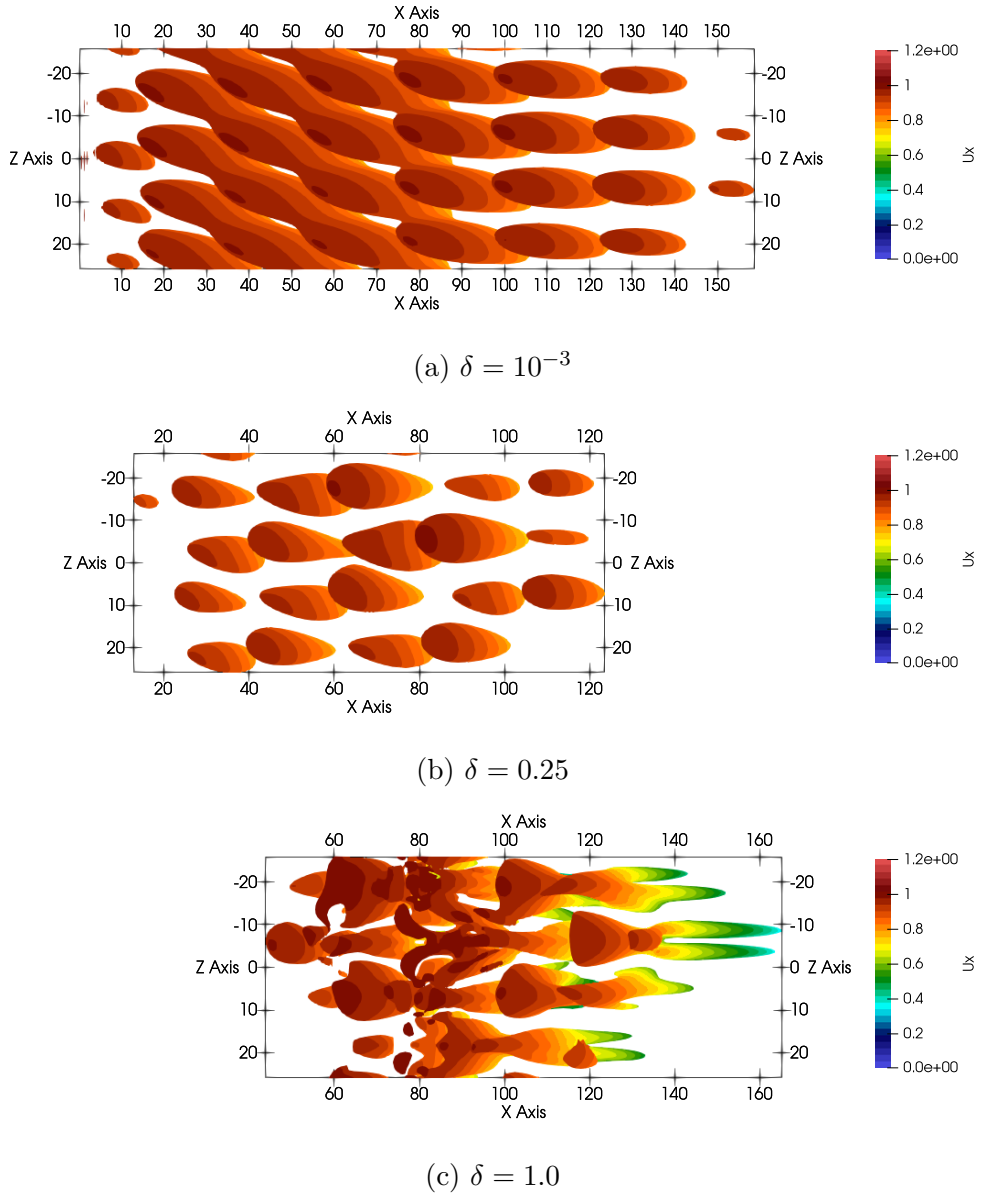
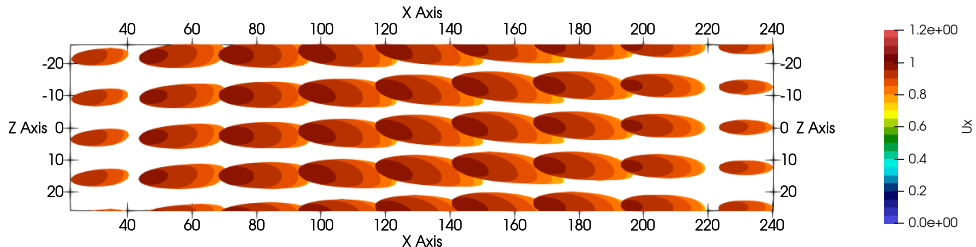
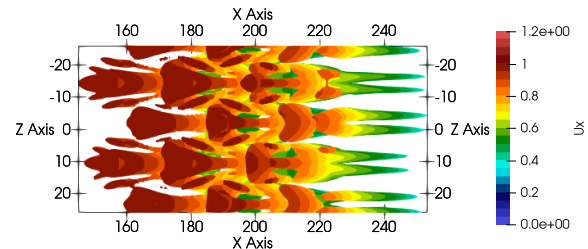


FIG. 5: Isosurfaces of the second invariant of the velocity gradient tensor (Q -criterion) at 0.001 of the optimal perturbation at $t_f = 150$ under the adiabatic wall temperature. The color contour shows the velocity distribution of the base flow field.

compressible results (see Fig. 6 in [25]), the spatial distribution in the present study differs significantly, characterized by the flattened distribution at the maximum shear layer and the long tails of vortices near the wall. Despite these structural discrepancies, the fundamental conclusions regarding nonlinear non-modal analysis reported by [25] are expected to hold for supersonic boundary layers, as discussed in the following section.



(a) $\delta = 10^{-3}$



(b) $\delta = 1.0$

FIG. 6: The case at cooled boundary wall at $T_w = 0.6T_{\text{ad.}}$ in the same manner of Fig. 5.

Under the wall-cooled condition ($T_w = 0.6T_{\text{ad.}}$), the characteristics of the optimal perturbations described above are almost entirely reproduced. The primary differences in the spatial distribution are a downward shift in the streamwise distribution ($x \in [140, 240]$ at $\delta = 1.0$ based on the energy criteria) and the associated nonlinear effects, as illustrated in Fig. 6. In this figure, the nonlinear optimal perturbation maintains an orderly spanwise symmetry. This suggests that a larger initial disturbance amplitude is required to break this symmetric pattern compared to the adiabatic case ($T_w = T_{\text{ad.}}$), a result consistent with the fact that wall cooling typically stabilizes the boundary layer.

The similarity of optimal perturbations in Fig. 5 and Fig. 6 suggests that the disappearance of the GIP due to the wall cooling does not significantly affect the spatial structure of the optimal perturbation. This is expected, given that the linear optimal perturbations in local theory are composed by the pseudospectra of the linear stability operator [16]. While the suppression of Mack's first mode by wall cooling leads to a decrease in the linear amplification of the disturbance field (as shown in Table. I), the rapid increase in nonlinear growth for the cooled wall indicates that the underlying nonlinear amplification mechanism is not significantly suppressed by the absence of the GIP. Therefore, we conclude that accounting for nonlinearity is critical for predicting laminar-to-turbulent transition, particularly under

wall-cooled conditions where linear theories may underestimate the transition potentials.

V. EVOLUTION OF THE PERTURBED FLOW

In this section, we consider the time-evolution of the disturbance field. Figure 7 displays the temporal evolution of the disturbance magnitude for various amplitudes δ and evaluation time t_f . The linear optimal perturbation ($\delta = 10^{-3}$) shows a clear dependence on t_f , with transient amplification observed in all cases. In the nonlinear case ($\delta = 1.0$), however, the long-term amplification characteristics vary significantly depending on the selection of t_f . Specifically, the optimal disturbance optimized for $t_f = 50$, which exhibits two-dimensional characteristics, eventually decays. In contrast, disturbances optimized for longer horizons continue to amplify over an extended period, eventually leading to a turbulent state. This transition is verified by a sustained increase in wall friction within the disturbed region (not shown here).

This sustained growth in the nonlinear regime is primarily attributed to finite-amplitude effects. To demonstrate this, the linear optimal perturbation was scaled by a constant to match the initial amplitude of the nonlinear case (see the dashed lines in Fig. 7 (b)). While this scaled linear perturbation also exhibits an increase in magnitude over time, its amplification rate is significantly lower than that of the true nonlinear optimal perturbation. This discrepancy suggests that the spatial redistribution of the disturbance field, as illustrated in Fig. 5, plays a crucial role in enhancing nonlinear growth. A more detailed comparison between the transition induced by the nonlinear optimal perturbation and that triggered by a finite-amplitude linear perturbation is presented in the next section.

Then, we consider the effect of the initial disturbance magnitude on the temporal evolution of the disturbance field, specifically for the case of $t_f = 150$. Figure 8 compares the evolution of linear and nonlinear optimal perturbations, where the initial amplitude of linear case is scaled to match the nonlinear cases. As shown in the figure, the linear optimal perturbation exhibits an upwardly convex growth curve, indicating that the linear non-modal growth mechanism persists even at finite amplitudes.

For the scaled optimal perturbation, nonlinear amplification is observed when $\delta > 0.5$, where nonlinear interactions emerge with the finite-amplitude disturbance field. In the case of the nonlinear optimal perturbation, a small disturbance amplitude ($\delta = 0.1$) shows no

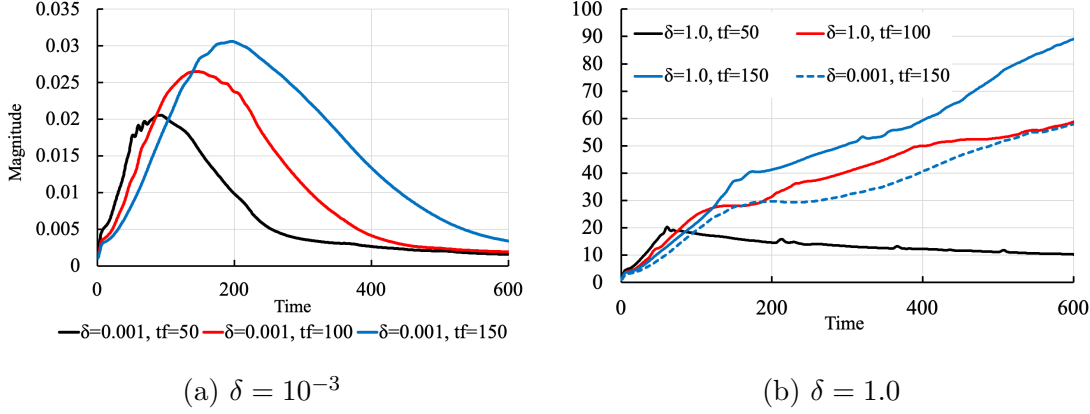


FIG. 7: Time-evolution of the disturbance magnitude at different δ, t_f . The dashed line indicates the linear optimal perturbation when its initial amplitude was adjusted to

$$\delta = 1.0.$$

significant deviation from the scaled linear counterpart, as expected by the growth rate in Table II. As δ increases, the initial evolution stage of the nonlinear optimal perturbation remains similar to the scaled linear case, albeit with a slight increase in disturbance magnitude. However, the subsequent temporal evolution shows a marked increase compared to the linear counterpart. This supports the conclusion that the nonlinear optimal perturbation initially triggers nonlinear interactions within the linearly amplified disturbance field. Further increases in δ lead to significant amplification even at the earliest stages, resulting in a rapid growth in disturbance magnitude. The threshold initial amplitude for transition is found to be $0.4 < \delta < 0.5$, above which the minimal seed to trigger the transition is obtained. This demonstrates that our nonlinear analysis identifies a more efficient and rapid amplification path by exploiting the finite-amplitude dynamics of the disturbance field.

We then consider the temporal evolution of the flow field perturbed by a finite-amplitude linear optimal perturbation. Figure 9 displays the spatial distribution of isosurfaces for the second invariant of the velocity gradient tensor (Q -criterion). In the evolution of the linear optimal perturbation, we observe the staggered pattern of streamwise vortices. This pattern originates from the initial spatial distribution of the linear optimal perturbation, as previously shown in Fig. 5 (a). This staggered vortex arrangement induces the formation of streaks and their subsequent breakdown, as illustrated in Fig. 9, accompanied by rope-like structure in the spanwise vorticity distribution. These features indicate that the transition process induced by the linear optimal perturbation exhibits strong similarities to the oblique

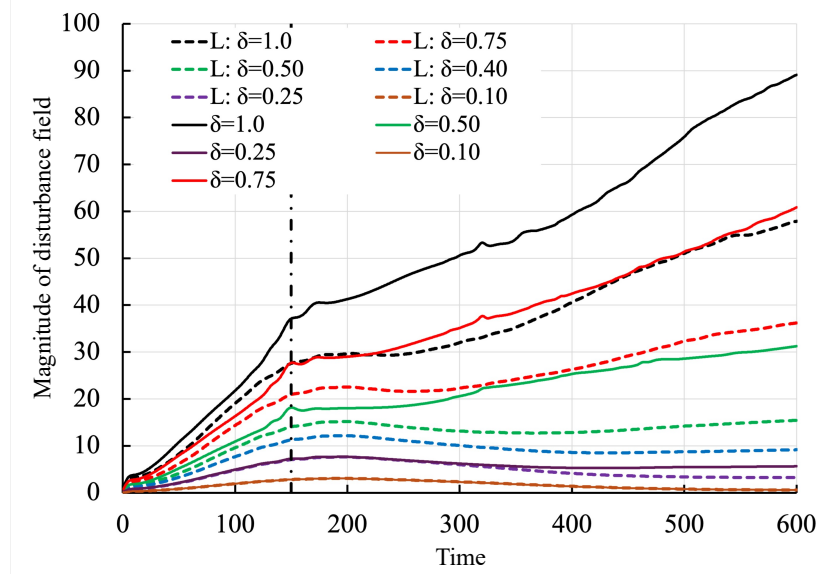


FIG. 8: Time evolution of the disturbance magnitude for the linear (L) and nonlinear optimal perturbation field, where linear optimal perturbation was obtained at $\delta = 10^{-3}$.

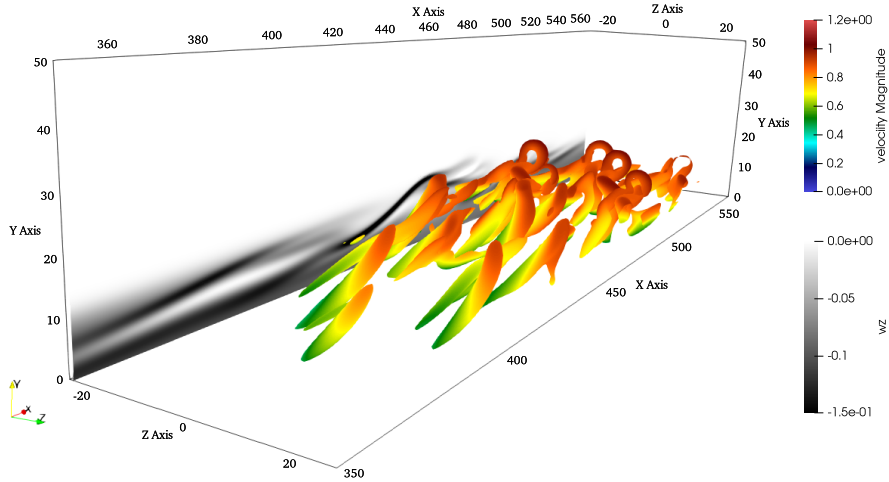


FIG. 9: Isosurfaces of the second invariant of the velocity gradient tensor (Q -criterion) at 2.0×10^{-4} of the perturbed flow field by the finite amplitude of linear optimal perturbation estimated with $t_f = 150, \delta = 0.001$ under the adiabatic wall temperature. The color contour indicates the velocity magnitude of the perturbed flow field and the projection view shows the spanwise vorticity.

breakdown scenario in supersonic boundary layer, as discussed by Mayer et al. (2011) [8].

Next, we investigate the physical mechanism of the laminar-to-turbulent transition induced by nonlinear optimal perturbation. Figure 10 displays the isosurfaces of the Q -

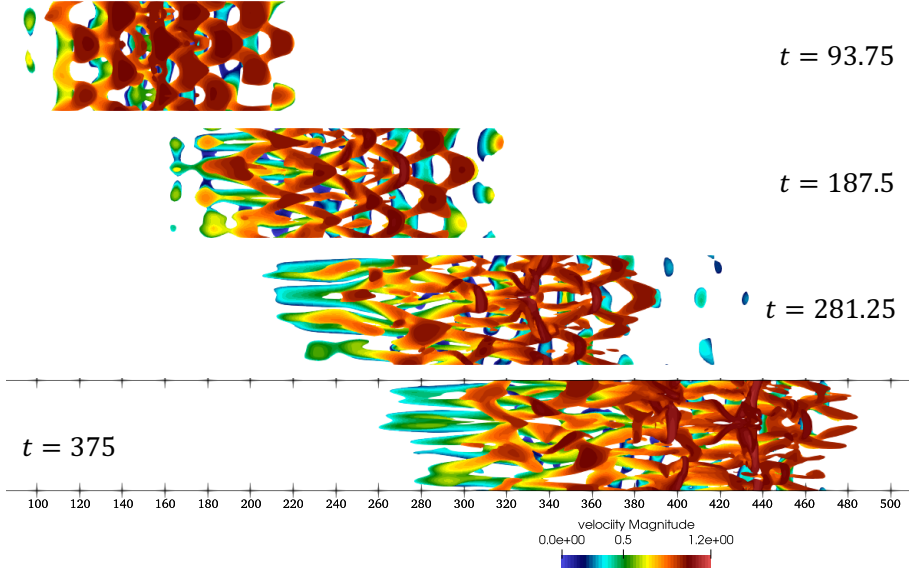


FIG. 10: Isosurfaces of the second invariant of the velocity gradient tensor (Q -criterion) at 10^{-6} of the perturbed flow field by the optimal perturbation estimated with $t_f = 150, \delta = 1.0$ under the adiabatics wall temperature. The color contour indicates the magnitude of the velocity of the perturbed flow field.

criterion for the perturbed flow field. Visual inspection reveals that the nonlinear interaction between two-dimensional planar waves in the near-wall region and staggered vortex pattern of oblique waves in the outer layer ($t = 93.75$) leads to the formation of streamwise vortices ($t = 281.25$). While the formation of a staggered vortex pattern is a hallmark of oblique breakdown [22], we observe that the presence of planar waves near the wall accelerates the rapid deformation of these vortices. This process is driven by streamwise stretching and the self-induction of Λ -shaped vortices, consistent with the mechanism discussed by Adams and Kleiser(1996) [11] for supersonic boundary layer. This interaction eventually results in the rapid formation of streaks via the self-induction of the vortex structures.

To characterize this structural evolution quantitatively, we analyzed the Reynolds stress. Figure 11 shows the wall-normal distribution of Reynolds stress components, averaged within a frame of reference moving with the turbulent spot. The streamwise averaging domain was initially defined as $x \in [140, 180]$ at $t = 93.8$ and was convected downstream at the spot's mean group velocity, $u_g = 0.871$. This velocity was determined from the convective speed of the primary skin-friction peak at the leading edge of the turbulent spot. We confirmed that the results are robust with respect to the choice of the averaging domain.

During the early stage ($t \leq 140.6$), $\overline{u'_x u'_x}$ exhibits a single peak that shifts toward the wall over time. This is accompanied by a peak in $\overline{u'_y u'_y}$, supporting the scenario of streak amplification via vortex self-induction. At later times, a second peak emerges in both $\overline{u'_x u'_x}$ and $\overline{u'_z u'_z}$ away from the wall, reflecting the lift-up mechanism of the streaks. Comparing these results with the three-dimensional structures shown in Fig. 10, this outer peak corresponds to the heads of the Λ -vortices. Furthermore, the flattened profile of $\overline{u'_y u'_y}$ in Fig. 11 (b) suggests the breakdown into smaller-scale vortices. This temporal evolution of the Reynolds stress is closely related to the findings reported by Adams and Kleiser (1996) [11], indicating that the late stage of turbulence does not differ significantly from that induced by the linear optimal perturbation, and by extension, the oblique breakdown scenario. Consequently, the transition process is uniquely characterized by the streak formation driven by vortex self-induction in its early stage.

The flow field observed in the late stages of the disturbance evolution exhibits characteristics typical of the oblique wave breakdown process. This accounts for the similar growth rates observed for both the linear and nonlinear optimal perturbations at $\delta = 1.0$, particularly for $t \geq 400$ as shown in Fig. 8. Furthermore, Figs. 9 and 10 (specifically at $t = 375$) demonstrate the formation of Λ -shape vortices as the primary structures driving the transition to turbulence. These features indicate that the nonlinear optimal perturbation identifies an accelerated amplification path for finite-amplitude disturbances. Consequently, the resulting transition mechanism should be interpreted as an extension of the oblique breakdown scenario, optimized for rapid growth in the nonlinear regime.

VI. CONCLUSION

In this study, the nonlinear amplification of the disturbance field for supersonic boundary layer at $M = 3.0$, $Re = 300$ based on the Blasius length is investigated using nonlinear non-modal analysis. The analysis focused on the initial stage of disturbance amplification, examining the effects of evaluation time (t_f), initial disturbance amplitude (δ) and wall temperature (T_w). As the initial disturbance amplitude increases from linear regime, the optimal perturbation initially extracts secondary nonlinear interactions that follow the linear amplification mechanism. Beyond a critical threshold of the initial amplitude, the nonlinear optimal perturbation identified transition paths governed by finite-amplitude dynamics.

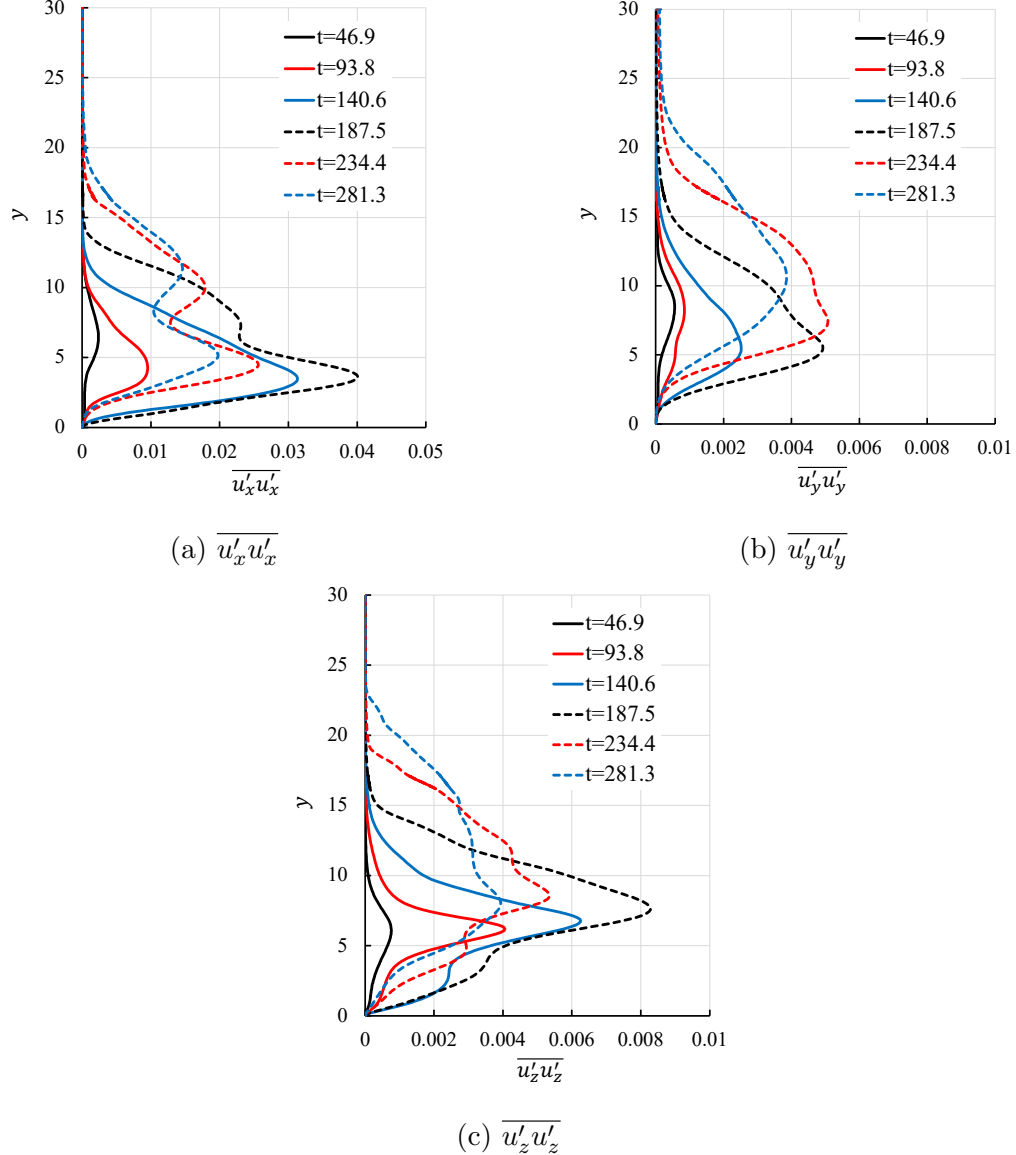


FIG. 11: Wall-normal distribution of the principal components of Reynolds stress averaged in a moving coordinates near the forward front of turbulent spot.

These paths are characterized by a flattened distribution in the upper boundary layer and streamwise vortices near the wall. Under the wall-cooling condition, this finite-amplitude structures persists while the subsonic inviscid instability suppressed by the disappearance of generalized inflection point, which may lead to an underestimation of transition prediction based on linear stability theory.

A key conclusion of the present study is that the nonlinear optimal perturbation induces rapid amplification of the finite-amplitude disturbance field during the initial stage,

while the late-stage evolution remains governed by the physical mechanism of oblique breakdown. The wall-normal expansion of the disturbance within the boundary layer facilitates a rapid transition by forming streaks through a vortex self-induction mechanism. This mechanism arises from the nonlinear interaction between the staggered vortex distribution in the outer boundary layer and the near-wall planar structures. These nonlinear processes trigger laminar-to-turbulent transition at significantly lower initial disturbance amplitudes than predicted by linear theory, a finding consistent with the role of nonlinear amplification in incompressible flows reported by Cherubini et al. [25].

- [1] L. Lees and C. C. Lin, Investigation of the stability of the laminar boundary layer, Tech. Rep., NACA-TN-1115 (1946).
- [2] L. Lees and E. Reshotko, Stability of the compressible laminar boundary layer, *Journal of Fluid Mechanics* **12**, 555 (1962).
- [3] L. M. Mack, Boundary-layer linear stability theory, Tech. Rep., DTIC Document (1984).
- [4] L. M. Mack, On the inviscid acoustic-mode instability of supersonic shear flows: Part 1: Two-dimensional waves, *Theoretical and Computational Fluid Dynamics* **2**, 97 (1990).
- [5] K. Stetson and R. Kimmel, On hypersonic boundary-layer stability, in *30th aerospace sciences meeting and exhibit* (1992) p. 737.
- [6] C.-L. Chang and M. R. Malik, Oblique-mode breakdown and secondary instability in supersonic boundary layers, *Journal of Fluid Mechanics* **273**, 323 (1994).
- [7] N. Sandham, N. A. Adams, and L. Kleiser, Direct simulation of breakdown to turbulence following oblique instability waves in a supersonic boundary layer, *Applied scientific research* **54**, 223 (1995).
- [8] C. S. Mayer, D. A. Von Terzi, and H. F. Fasel, Direct numerical simulation of complete transition to turbulence via oblique breakdown at Mach 3, *Journal of Fluid Mechanics* **674**, 5 (2011).
- [9] A. N. Kudryavtsev and D. V. Khotyanovsky, Direct numerical simulation of transition to turbulence in a supersonic boundary layer, *Thermophysics and Aeromechanics* **22**, 559 (2015).
- [10] S. Berlin, M. Wiegel, and D. S. Henningson, Numerical and experimental investigations of oblique boundary layer transition, *Journal of Fluid Mechanics* **393**, 23 (1999).

- [11] N. A. Adams and L. Kleiser, Subharmonic transition to turbulence in a flat-plate boundary layer at Mach number 4.5, *Journal of Fluid Mechanics* **317**, 301 (1996).
- [12] A. Kosinov, A. Maslov, and S. Shevelkov, Experiments on the stability of supersonic laminar boundary layers, *Journal of Fluid Mechanics* **219**, 621 (1990).
- [13] C. Mayer and H. Fasel, Investigation of asymmetric subharmonic resonance in a supersonic boundary layer at Mach 2 using DNS, in *46th AIAA Aerospace Sciences Meeting and Exhibit* (2008) p. 591.
- [14] L. L. Ng and G. Erlebacher, Secondary instabilities in compressible boundary layers, *Physics of Fluids A: Fluid Dynamics* **4**, 710 (1992).
- [15] Y. Zhu, C. Zhang, X. Chen, H. Yuan, J. Wu, S. Chen, C. Lee, and M. Gad-el Hak, Transition in hypersonic boundary layers: Role of dilatational waves, *AIAA Journal* **54**, 3039 (2016).
- [16] L. N. Trefethen, A. E. Trefethen, S. C. Reddy, and T. A. Driscoll, Hydrodynamic stability without eigenvalues, *Science* **261**, 578 (1993).
- [17] S. C. Reddy and D. S. Henningson, Energy growth in viscous channel flows, *Journal of Fluid Mechanics* **252**, 209 (1993).
- [18] A. Hanifi, P. J. Schmid, and D. S. Henningson, Transient growth in compressible boundary layer flow, *Physics of Fluids* **8**, 826 (1996).
- [19] A. Tumin and E. Reshotko, Spatial theory of optimal disturbances in boundary layers, *Physics of Fluids* **13**, 2097 (2001).
- [20] B. Bugeat, J.-C. Chassaing, J.-C. Robinet, and P. Sagaut, 3D global optimal forcing and response of the supersonic boundary layer, *Journal of Computational Physics* **398**, 108888 (2019).
- [21] P. Paredes, M. M. Choudhari, and F. Li, Instability wave–streak interactions in a supersonic boundary layer, *Journal of Fluid Mechanics* **831**, 524 (2017).
- [22] A. Poulain, C. Content, G. Rigas, E. Garnier, and D. Sipp, Adjoint-based linear sensitivity of a supersonic boundary layer to steady wall blowing–suction/heating–cooling, *Journal of Fluid Mechanics* **978**, A16 (2024).
- [23] S. Cherubini, P. De Palma, J.-C. Robinet, and A. Bottaro, Rapid path to transition via nonlinear localized optimal perturbations in a boundary-layer flow, *Physical Review E* **82**, 066302 (2010).
- [24] C. C. Pringle and R. R. Kerswell, Using nonlinear transient growth to construct the minimal

seed for shear flow turbulence, *Physical review letters* **105**, 154502 (2010).

[25] S. Cherubini, P. De Palma, J.-C. Robinet, and A. Bottaro, The minimal seed of turbulent transition in the boundary layer, *Journal of Fluid Mechanics* **689**, 221 (2011).

[26] Z. Huang and M. P. Hack, A variational framework for computing nonlinear optimal disturbances in compressible flows, *Journal of Fluid Mechanics* **894** (2020).

[27] R. Jahanbakhshi and T. A. Zaki, Nonlinearly most dangerous disturbance for high-speed boundary-layer transition, *Journal of Fluid Mechanics* **876**, 87 (2019).

[28] T. Zhou, Z. Liu, Y. Lu, and C. Yan, Interactions between oblique second mode and oblique waves in a high-speed boundary layer, *Journal of Fluid Mechanics* **973**, A27 (2023).

[29] G. Rigas, D. Sipp, and T. Colonius, Nonlinear input/output analysis: application to boundary layer transition, *Journal of Fluid Mechanics* **911**, A15 (2021).

[30] M. R. Malik, Numerical methods for hypersonic boundary layer stability, *Journal of computational physics* **86**, 376 (1990).

[31] N. Taniguchi, Y. Ohmichi, and K. Suzuki, Nonlinear transient disturbance growth analysis for the compressible external flow and application to a flow around circular cylinder, *Journal of Computational Physics* **516**, 113374 (2024).

[32] Y. Ohmichi and K. Yamada, Matrix-free triglobal adjoint stability analysis of compressible Navier-Stokes equations, *Journal of Computational Physics* **437**, 110332 (2021).

[33] C. C. Pringle, A. P. Willis, and R. R. Kerswell, Minimal seeds for shear flow turbulence: using nonlinear transient growth to touch the edge of chaos, *Journal of Fluid Mechanics* **702**, 415 (2012).

[34] Y. Duguet, A. Monokrousos, L. Brandt, and D. S. Henningson, Minimal transition thresholds in plane couette flow, *Physics of Fluids* **25** (2013).

[35] S. Kawai and K. Fujii, Compact scheme with filtering for large-eddy simulation of transitional boundary layer, *AIAA journal* **46**, 690 (2008).

[36] D. J. Bodony, Analysis of sponge zones for computational fluid mechanics, *Journal of Computational Physics* **212**, 681 (2006).

[37] S. K. Lele, Compact finite difference schemes with spectral-like resolution, *Journal of computational physics* **103**, 16 (1992).

[38] D. V. Gaitonde and M. R. Visbal, Padé-type higher-order boundary filters for the Navier–Stokes equations, *AIAA journal* **38**, 2103 (2000).

- [39] S. Gottlieb and C.-W. Shu, Total variation diminishing Runge-Kutta schemes, *Mathematics of computation* **67**, 73 (1998).
- [40] F. M. White, *Viscous fluid flow*, McGraw-Hill New York (1991).
- [41] S. Cherubini and P. De Palma, Nonlinear optimal perturbations in a Couette flow: bursting and transition, *Journal of Fluid Mechanics* **716**, 251 (2013).
- [42] R. Kerswell, Nonlinear nonmodal stability theory, *Annual Review of Fluid Mechanics* **50**, 319 (2018).
- [43] A. Dwivedi, N. Hildebrand, J. W. Nichols, G. V. Candler, and M. R. Jovanović, Transient growth analysis of oblique shock-wave/boundary-layer interactions at Mach 5.92, *Physical Review Fluids* **5**, 063904 (2020).